Effect of Heat Treatment on the Photoluminescent and Structural Properties of Europium-Doped Yttrium Oxide

María de Jesús Martínez-Carreón (https://orcid.org/0000-0002-9283-7857)[a]*, Raquel Murillo-Ortiz (https://orcid.org/0009-0007-4377-6107)[a], Azael Adrián Cavazos-Jaramillo (https://orcid.org/0000-0003-0728-7094)[b], María Magdalena Del Ángel-Sánchez (https://orcid.org/0009-0002-9241-5117)[c], Mitchel Abraham Ruiz-Robles (https://orcid.org/0000-0003-4834-8025)[a] y Eduardo G. Pérez-Tijerina (https://orcid.org/0000-0001-9742-4093)[a]

[a] *CICFM, Facultad de Ciencias Físico Matematicas, Universidad Autónoma de Nuevo Lean, Av. Universidad s/n, San Nicolas de los Garza, México.*
[b] *Facultad de Ciencias Biológicas, Universidad Autonoma de Nuevo Leon, Av. Universidad s/n, San Nicolás de los Garza, México.*
[c] *Universidad Tecnologica Gral. Mariano Escobedo (UTE), Libramiento Noreste Km. 33.5, General Escobedo, Nuevo Leon. C.P. 66050.*
* *maria.martinezcr@uanl.edu.mx*

Recibido: 15 de mayo de 2026, Aceptado 10 de junio de 2026

Abstract
The synthesis and characterization analysis of as-synthesized and heat-treated of europium-doped yttrium oxide $(Eu_{0.04}Y_{0.96})_2O_3$ powders was performed using photoluminescence, X-ray diffraction, SEM, energy-dispersive X-ray spectroscopy, AES, and XPS. The results demonstrated a 12.5-fold increase in luminescent intensity after heat treatment at 1273 K for 30 min compared to as-synthesized powders measured at 273 K. XRD revealed that as-synthesized powders exhibited a high degree of lattice strain, which was substantially relieved upon thermal treatment, resulting in notably sharper and more defined peaks indicative of improved crystallinity. SEM analysis correlated the enhanced PL intensity with a reduction in crystallite size post-heat-treatment, suggesting morphological optimization contributes to superior luminescence properties. EDS spectra confirmed the presence of only Eu, O and Y in both as-synthesized and heat-treated samples, with no detectable impurity elements. Notably, the emergence of a europium signal in the AES spectrum of heat-treated powders strongly suggests an increase in europium incorporation or surface concentration following the 1273 K treatment for 30 min, providing a mechanistic insight into the observed PL enhancement.
Keywords: Yttrium oxide, Europium, Heat treatment, Characterization methods.

Resumen
Se realizó la síntesis y análisis de polvos de óxido de itrio dopado con europio $(Eu_{0.04}Y_{0.96})_2O_3$ recién sintetizados y tratados térmicamente utilizando fotoluminiscencia, DRX, MEB, espectroscopía de dispersión de energía de rayos X, espectroscopía de electrones Auger y XPS. Los resultados demostraron un aumento de 12.5 veces en la intensidad luminiscente después del tratamiento térmico a 1273 K durante 30 min, en comparación con polvos recién sintetizados medidos a 273 K. La DRX reveló que los polvos recién sintetizados exhibían un alto grado de tensión en la red cristalina, la cual se alivió sustancialmente con el tratamiento térmico, resultando en picos notablemente más agudos y definidos, indicativos de una cristalinidad mejorada. El análisis por MEB correlacionó el aumento en la intensidad de PL con una reducción en el tamaño de los cristalitos tras el tratamiento térmico, sugiriendo que la optimización morfológica contribuye a propiedades de luminiscencia superiores. Los espectros EDS confirmaron la presencia solo de Eu, O e Y en ambas muestras recién sintetizadas y tratadas térmicamente, sin elementos de impureza detectables. Notablemente, la aparición de una señal de europio en el espectro AES de los polvos tratados térmicamente sugiere fuertemente un aumento en la incorporación de europio o en su concentración superficial tras el tratamiento a 1273 K durante 30 min, proporcionando una explicación mecanicista para el aumento observado en la PL.
Palabras clave: óxido de itrio, Europio, Tratamiento térmico, Métodos de caracterización.

1. Introduction

Due to its exceptional optical properties, yttrium oxide doped with rare-earth elements has garnered significant attention, making it a crucial component for a variety of applications, such as phosphors, solid-state lasers, and optical sensors [1,2]. Specifically, the europium-doped Y_2O_3 nanophosphors have higher surface to volume ratios and increased photoluminescence due to quantum confinement effects, making them ideal for sophisticated optical and electronic devices [3].

In rare-earth-doped yttrium oxide, thermal treatments have been shown to significantly improve crystallinity and mitigate structural defects, which are important factors in maximizing luminescence intensity through the reduction of non-radiative recombination routes [4-6]. For example, increased photoluminescence emission in Yttrium Europium Oxides (Y_2O_3: Eu^{3+}) materials has been linked

to improvements in crystallite size and phase purity caused by thermal annealing [7].

Moreover, precise modulation of post-synthesis thermal parameters, such as annealing temperature and atmospheric conditions, exerts profound effects on the optical and morphological properties of these materials, as substantiated by research on nanophosphors [8,9] and ultrathin films [6].

2. Experimental Details

2.1 Synthesis of Luminescent Materials

Combustion synthesis is a wet chemical reaction that utilizes an exothermic reaction between precursor components. This reaction occurs rapidly and self-sustainably between a carbonaceous fuel and metal nitrates, with the fuel type and fuel-to-nitrate ratio serving as the primary parameters controlling the reaction temperature. In a typical combustion reaction, the precursor mixture, diluted in a small amount of water, is placed in a low temperature muffle, where it dehydrates and ignites into a flame within about 5 to 10 minutes. As an example, the reaction for is shown below:

$$a_x Eu(NO_3)_3 + b_{1-x} Y(NO_3)_3 + cCH_6N_4O \rightarrow d(Eu_xY_{1-x})_2O_3 + eN_2 + fH_2O + gCO_2 + hO_2$$

In this study, 4% europium-doped Y_2O_3 was synthesized via combustion. Stoichiometric amounts of yttrium nitrate, europium nitrate, and carbohydrazide (used as fuel with a 30% excess) were dissolved in deionized water. The reagents were mixed and stirred at room temperature for 20 minutes before being transferred to a muffle furnace preheated to 773 K, where the combustion reaction completed in 10 minutes or less, yielding a foamy material. Subsequently, the sample was calcined at 1273 K for 30 minutes to enhance its crystallization and luminescent properties.

2.2 Characterization

Photoluminescence measurements were performed using a Hitachi fluorescence spectrophotometer model F-4500 equipped with a UV-IR Xe lamp. As-synthesized powders (after combustion at 773 K) were excited at 275 nm, while heat-treated powders (at 1273 K) were excited at 254 nm.

X-ray Diffraction analysis was conducted using a PANalytical diffractometer model X'Pert PRO at 40 kV and 40 mA with Cu Kα radiation at a scan speed of 2°/min.

Chemical composition and surface morphology were characterized by Scanning Electron Microscopy on a JEOL JSM-5300 microscope operated at 15 keV, equipped with EDS detector.

Transmission Electron Microscopy micrographs were obtained using a JEOL JEM-2010 microscope at 200 keV accelerating voltage and a base pressure of 1×10^{-5} Pa.

Auger Electron Spectroscopy (AES) was carried out on a PHI 595 spectrometer with primary electron beam energies of 3 and 5 keV. Surfaces were sputter-etched using Ar^+ ions at 1.3×10^{-9} Torr. Samples were prepared by impurity removal at atmospheric pressure in the introduction chamber, followed by pumping to 1×10^{-6} Torr (~2 h), then transfer to the ultra-high vacuum analysis chamber. Positioning ensured focused Auger electrons on the detector, calibrated via AugerScan software to center the elastic peak. Spectra from 20–1000 eV and 30–1800 eV optimized ionization cross-section signals; first derivatives minimized resolution related errors despite decreasing detector performance at elevated energies.

X-ray photoelectron spectroscopy was performed on a Leybold LHS-18 system (base pressure 1×10^{-9} Torr) using an Al Kα source. Pass energy was 200 eV, with 1.5 eV steps, 0.1 s dwell time, 10 scans, and a 0–1200 eV binding energy window.

3. Results and Discussion

3.1 Photoluminescence Properties

The photoluminescence emission spectra were measured for both the as-synthesized sample and the powders thermally treated at 1273 K for 30 min. Figure 1 shows the emission spectrum of the as-synthesized $(Eu_{0.04}Y_{0.96})_2O_3$ sample. The spectrum is dominated by a sharp and intense emission peak at approximately 612–615 nm, characteristic of the $^5D_0 \rightarrow {}^7F_2$ electric dipole transition of Eu^{3+} ions. This hypersensitive transition, highly sensitive to the local symmetry of the Eu^{3+} environment, is definitively associated with intense red emission in rare-earth-doped oxides [10,11]. In addition to the main peak, weaker emission bands appear in the ~580–600 nm region, corresponding to the $^5D_0 \rightarrow {}^7F_1$ magnetic dipole transition. The lower intensity of this transition relative to the $^5D_0 \rightarrow {}^7F_2$ transition confirms that Eu^{3+} ions occupy sites without inversion symmetry within the Y_2O_3 host lattice [12,13].

The narrow linewidths and well-defined peaks clearly demonstrate that the as-synthesized material contains optically active Eu^{3+} centers. However, the overall emission intensity is moderate primarily due to structural defects, surface states, and residual impurities that promote non-radiative recombination [5, 14-15].

The dominance of the red emission band unequivocally confirms the successful incorporation of Eu^{3+} ions into the Y_2O_3 matrix [16] and demonstrates that combustion synthesis yields luminescent materials even without post-synthesis thermal treatment [17].

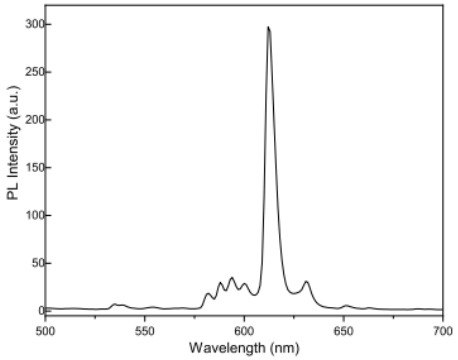

Figure 1. Emission spectrum for $(Eu_{0.04}Y_{0.96})_2O_3$ as-synthesized powders.

Figure 2 presents the photoluminescence excitation spectrum of the $(Eu_{0.04}Y_{0.96})_2O_3$ as-synthesized powders, monitored at the principal emission wavelength. The spectrum displays a broad, intense band centered at 270–280 nm, attributed to the O–Eu charge transfer [18]. This breadth reflects multiple local environments and structural disorder [19] consistent with low crystallinity and high defect density from SEM and XPS, while its high intensity indicates efficient host-lattice energy absorption and transfer to Eu [20], enabling the observed red emission. Slight asymmetry suggests surface states or defects influencing excitation [21]. At longer wavelengths, intensity decreases without resolved f–f transitions, masked by disorder and non-radiative processes [22]. Overall, the spectrum confirms charge transfer band (CTB) dominated luminescence in the oxide host [23], broadened by pre-treatment disorder.

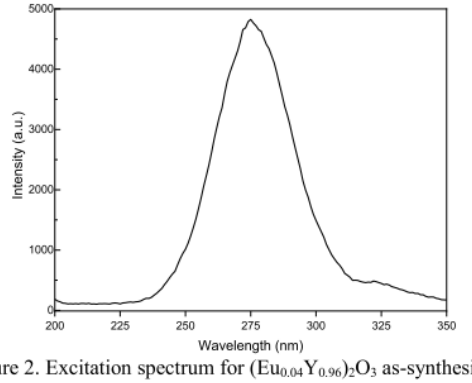

Figure 2. Excitation spectrum for $(Eu_{0.04}Y_{0.96})_2O_3$ as-synthesized powders.

The PL emission spectrum of $(Eu_{0.04}Y_{0.96})_2O_3$ powders following a 30-minute thermal treatment at 1273 K is shown in Figure 3. Because of better crystallinity, fewer defects, and the elimination of residual carbon and quenching impurities, the emission intensity is much higher than in the as-synthesized sample. With weaker bands at ~580–600 nm ($^5D_0 \rightarrow {}^7F_1$ magnetic dipole transition), the spectrum is dominated by a sharp, intense peak at ~612–615 nm ($^5D_0 \rightarrow {}^7F_2$ electric dipole transition of ions), which is responsible for the distinctive red emission. Eu ions occupy non-centrosymmetric sites in the lattice, as confirmed by the high intensity ratio.

A more uniform crystal field is reflected in the sharper and better-resolved peaks.

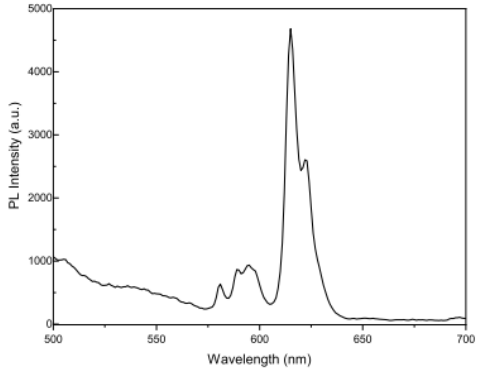

Figure 3. Emission spectrum for $(Eu_{0.04}Y_{0.96})_2O_3$ powders after heat treatment

Figure 4 shows the photoluminescence excitation spectrum of $(Eu_{0.04}Y_{0.96})_2O_3$ after thermal treatment, monitored at the main emission wavelength. The spectrum features a broad, intense band centered at 260–280 nm, attributed to the O–Eu CTB. Compared to the as-synthesized sample, this band is more intense, better defined, and narrower, indicating enhanced crystalline, reduced structural disorder, and a more homogeneous local environment around Eu ions. The heightened CTB intensity reflects efficient energy absorption and transfer from the host lattice to Eu centers, correlating with the stronger emission observed. Reduced broadening suggests fewer states related to surfaces and defects. Excitation intensity rapidly decreases above 300 nm without noticeable f–f transitions, indicating that CTB dominates intra-4f processes. Therefore, by reducing non-radiative pathways and stabilizing the Eu environment, annealing produces a more ordered luminescent system.

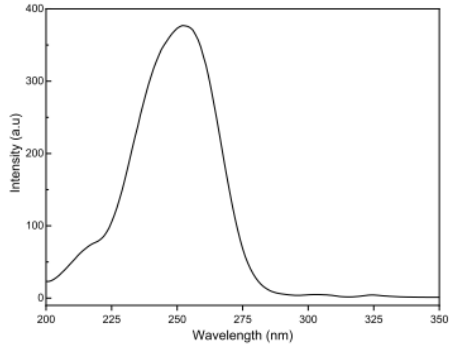

Figure 4. Excitation spectrum for $(Eu_{0.04}Y_{0.96})_2O_3$ powders after heat treatment

3.2 X-Ray Diffraction Analysis

The X-ray diffraction patterns of the $(Eu_{0.04}Y_{0.96})_2O_3$ powders in their as-synthesized state and heat treatment are shown in Figure 5, along with the reference pattern from the ICDD card that represents cubic Yttrium

Europium Oxide.

The XRD pattern of the as-synthesized material shows broad, low-intensity peaks that are suggestive of a partially amorphous or poorly crystalline phase.

The notable peak broadening is consistent with the fast, non-equilibrium conditions of the combustion synthesis process and reflects small crystallite sizes and a high degree of structural disorder [17]. Additionally, the low signal-to-noise ratio suggests that there may be defects and leftover species in the material.

The distinct, intense, and sharp diffraction peaks in the XRD pattern indicate a notable improvement in crystallinity after heat treatment. These changes exhibit notable grain growth and structural reorganization. The observed peaks' excellent agreement with ICDD card No. 00-025-1011 confirms the formation of a single-phase cubic Yttrium Europium Oxide structure with characteristic reflections corresponding to planes like (211), (222), (400), (440), and (622).

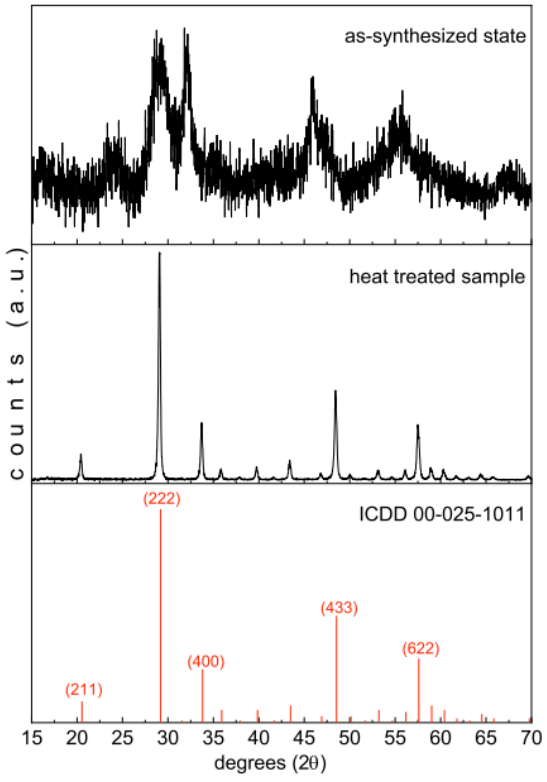

Figure 5. X-ray diffraction patterns of $(Eu_{0.04}Y_{0.96})_2O_3$ powders in the as-synthesized state, after annealing, and the corresponding ICDD crystallographic card.

The absence of extra peaks that might be linked to secondary phases or impurities indicates that the addition of Eu^{3+} ions to the Y_2O_3 lattice does not alter the crystal structure or result in phase segregation. This observation implies that because of their similar ionic radio, Eu^{3+} ions were successfully substituted at Y^{3+} sites.

Furthermore, the narrowing of diffraction peaks following annealing indicates a decrease in lattice strain and an increase in crystallite size. The predicted decrease of non-radiative recombination centers as a result of the enhanced crystallinity and structural ordering is directly linked to the increased photoluminescence observed in the emission spectra [14,22].

In conclusion, the XRD data show that the combustion-synthesized powders have low crystallinity at first, which is significantly enhanced by heat treatment, producing a distinct cubic Yttrium Europium Oxide phase with excellent structural quality and no discernible impurities.

3.3 Scanning Electron Microscopy and Energy Dispersive X-Ray Spectroscopy

The SEM micrographs reveal a pronounced morphological evolution in combustion-synthesized Y_2O_3:Eu powders upon thermal treatment at 1273 K for 30 min.

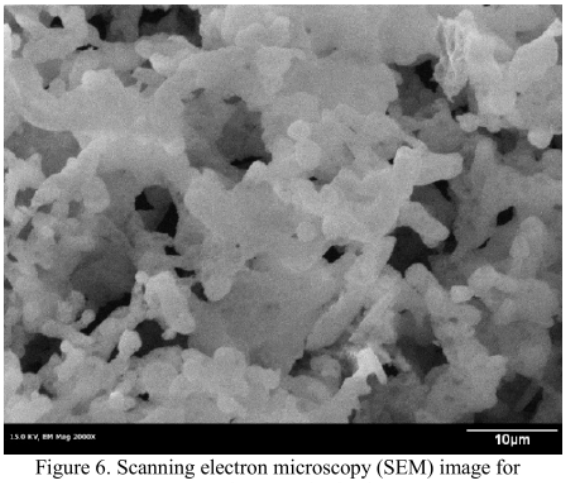

Figure 6. Scanning electron microscopy (SEM) image for sample as-synthesized

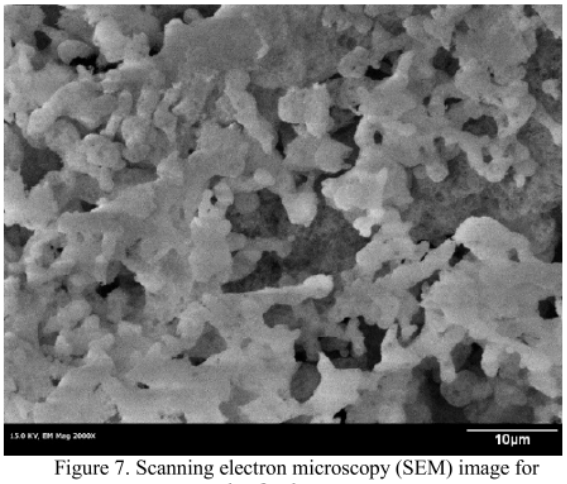

Figure 7. Scanning electron microscopy (SEM) image for sample after heat treatment

The material in the as-synthesized sample (Figure 6) has a highly porous, strongly agglomerated morphology of

irregular foam-like structures, which is typical of combustion synthesis, where a voluminous low-density network is formed by rapid exothermic reaction and gas evolution [24–25].

High specific surface area and poor crystallinity are indicated by the loosely packed aggregates of fine particles with many interparticle voids. The microstructure considerably densifies following thermal treatment (Figure 7), with agglomerates becoming more compact and well-defined and grains becoming more distinguishable as a result of increased atomic diffusion-driven particle growth and coalescence. As a result of void collapse and the removal of combustion byproducts, the foam-like porosity significantly decreases.

The elemental composition of combustion-synthesized Y_2O_3:Eu powders is confirmed by the EDS spectra, which are displayed in Figures 8 and 9 for the as-prepared state and after thermal treatment, respectively. No impurities were found. Peak intensities after treatment stay in line with the nominal composition, demonstrating chemical stability and the elimination of combustion by products.

Reproducible luminescent properties dependent on the environment are ensured by improved peak definition following annealing, which reflects improved crystallinity and homogeneity [26].

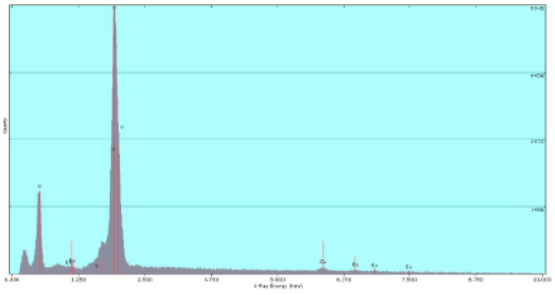

Figure 8. EDS spectrum for sample as-synthesized

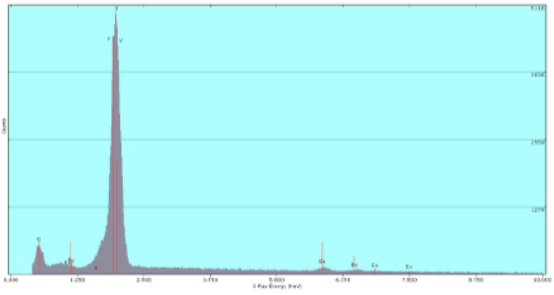

Figure 9. EDS spectrum for material after heat treatment

3.4 Auger Electron Spectroscopy

The surface chemical composition of the as-synthesised $(Eu_{0.04}Y_{0.96})_2O_3$ materials is revealed by the Auger electron spectroscopy spectrum, which shows distinctive derivative peaks for yttrium (prominent at lower kinetic energies), oxygen (strong signal at higher kinetic energies, consistent with the oxide matrix), and carbon.

Without suggesting bulk impurities, the carbon signal shows surface contamination [27–28], most likely from leftover organics from the combustion synthesis [29] typical for as-synthesized powders. Due to its low concentration and potential peak overlap with yttrium/oxygen, europium signals are undetectable [30, 31].

In line with EDS analysis, AES verifies a surface dominated by yttrium and oxygen with a small amount of carbon contamination.

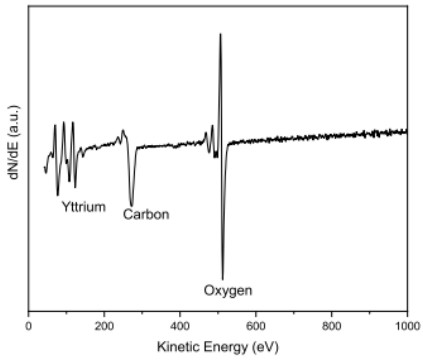

Figure 10. AES spectrum for the as-synthesized powders.

The sample's evolved surface chemical composition can be seen in the Auger electron spectroscopy spectrum following heat treatment (see Figure 11). It shows distinct derivative peaks for carbon, yttrium, oxygen, and europium. While prominent yttrium peaks appear sharper than in the as-synthesised sample, suggesting improved surface ordering and crystallinity, the strong oxygen signal at 510 eV validates the stability of the oxide framework. In comparison to the as-synthesised condition, the carbon signal at 270 eV is lower, indicating the removal of combustion residues. Due to decreased surface disorder that makes detection within the lattice easier, europium signals are now clearly visible at higher kinetic energies.

In line with SEM findings and favorable to increased luminescence, heat treatment results in a cleaner, more ordered surface with preserved composition and improved elemental resolution.

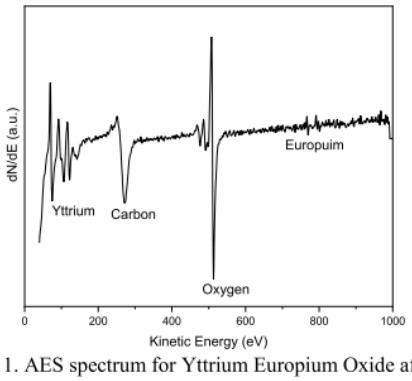

Figure 11. AES spectrum for Yttrium Europium Oxide after heat treatment

3.5 X-ray Photoelectron Spectroscopy

The near-surface elemental composition and oxidation states of the as-synthesized $(Eu_{0.04}Y_{0.96})_2O_3$ material are revealed by the X-ray photoelectron spectroscopy survey spectrum shown in Figure 12. It clearly confirms the formation of the Y_2O_3 matrix without detectable impurities from other elements, showing prominent core-level peaks for O 1s (530 eV), Y 3d (158 eV), and C 1s (285 eV).

The intense O 1s peak corresponds to lattice oxygen O^{2-} in Y_2O_3 reflecting the dominant surface oxygen content inherent to the clean oxide surface. The spin-orbit split $Y\ 3d_{5/2}$ and $Y\ 3d_{3/2}$ peaks (at 158-162 eV) precisely match yttrium in the Y^{3+} oxidation state characteristic of Y_2O_3 [16].

The C 1s peak arises from adventitious carbon and residual carbonaceous species stemming from the combustion synthesis—such as incomplete decomposition of organic fuels—or atmospheric adsorption [25, 28-29]. This surface carbon is ubiquitous in as-synthesized powders with high specific surface area and porosity, as observed in SEM [25], but does not indicate bulk contamination.

No distinct Eu core-level peaks are resolved, attributable to the low dopant concentration (4%), insufficient signal-to-noise ratio in survey mode, spectral overlap with Y/O signals, and the inherent surface sensitivity of XPS (~1-10 nm) [30]. Nevertheless, Eu incorporation is robustly corroborated by complementary EDS, AES, and high-resolution XPS results.

In summary, the XPS survey spectrum demonstrates a surface dominated by Y^{3+} and O^{2-} from pure Y_2O_3, with only minor C contamination and no impurity signals, attesting to the high chemical purity and successful combustion synthesis of Eu-doped Y_2O_3, in full agreement with prior XRD, SEM, EDS, and AES characterizations.

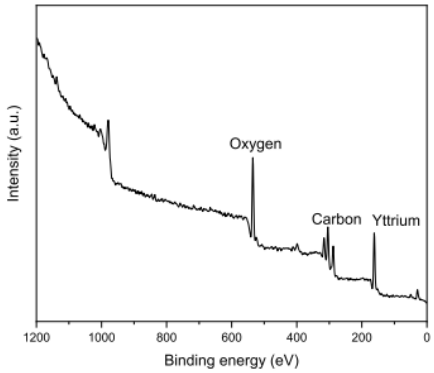

Figure 12. XPS spectrum for the as-synthesized sample.

Figure 13 presents the high-resolution XPS spectra of the C 1s, Eu 3d, O 1s, and Y 3d regions for the as-synthesized $(Eu_{0.04}Y_{0.96})_2O_3$ material, revealing the surface chemical states and composition.

The C 1s spectrum displays a main peak located at 284.8 eV characteristic of adventitious carbon (C–C/C–H). The asymmetry toward higher binding energies confirms oxidized carbon species, including C–O and O–C=O groups, arising from residual organics in the combustion synthesis or atmospheric adsorption—prevalent in as-synthesized powders [28]

The O 1s spectrum exhibits a broad, intense peak around 532–534 eV assigned to lattice oxygen O^{2-} in Y_2O_3 . Peak broadening confirms multiple oxygen environments, including lattice oxygen, hydroxyl groups, and adsorbed species, consistent with the porous, high-surface-area morphology observed by SEM [25].

The Y 3d spectrum reveals the characteristic spin-orbit doublet of $Y\ 3d_{5/2}$ and $Y\ 3d_{3/2}$ (158–163) eV, unequivocally confirming yttrium in the Y^{3+} oxidation state [16]. The broader peaks reflect structural disorder inherent to combustion-synthesized powders prior to annealing.

The Eu 3d spectrum, though weak due to the low dopant concentration (4%) and XPS surface sensitivity [30], displays discernible features at 1125–1135 eV corresponding to transitions, confirming successful incorporation into the host lattice [26]. Limited multiplet splitting resolution stems directly from low signal intensity.

In summary, high-resolution XPS confirms that the as-synthesized powder surface consists predominantly of Y_2O_3 with Y^{3+} and lattice/surface O^{2-}, minor carbon contamination from synthesis residues, and incorporated Eu^{3+}, fully consistent with EDS and AES results.

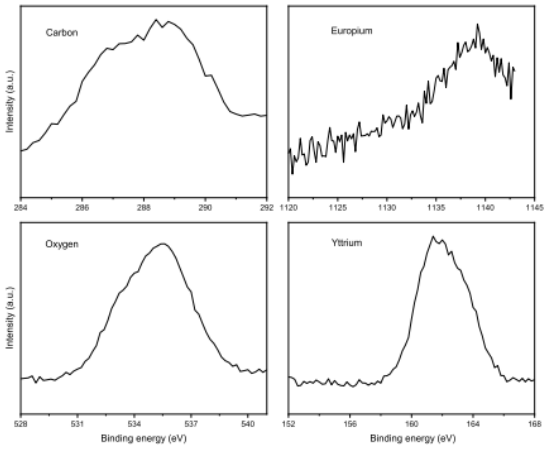

Figure 13. Individual XPS spectra for C, Eu, O and Y in the as-synthesized powders.

The XPS survey spectrum of the Y_2O_3:Eu powders after heat treatment at 1273 K for 30 min, presented in Figure 14, shows improved near-surface elemental composition. Prominent O 1s, Y 3d, and C 1s peaks confirm preservation and purification of the matrix [16].

The dominant O 1s peak (530 eV) is sharper and better defined than in the as-synthesized sample, indicating enhanced crystallinity and uniform chemical environment.

The Y 3d peaks for exhibit increased definition and intensity, reflecting structural ordering consistent with

SEM-observed grain growth and densification [25].

The C 1s peak shows reduced intensity, evidencing removal of combustion residues [28].

No impurity peaks appear, confirming chemical purity. Though unresolved due to low concentration and spectral overlap [30], europium is corroborated by AES and EDS.

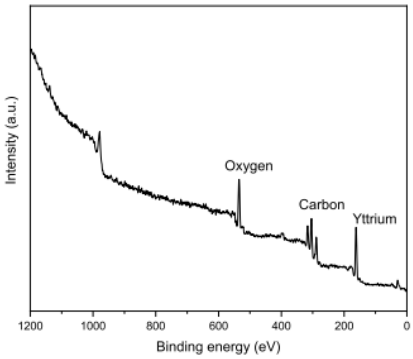

Figure 14. XPS spectrum for Yttrium Europium Oxide after heat treatment

High-resolution XPS spectra of the C 1s, Eu 3d, O 1s, and Y 3d regions for Y_2O_3:Eu powders following heat treatment are shown in Figure 15, which reveals refined surface chemical states and annealing effects.

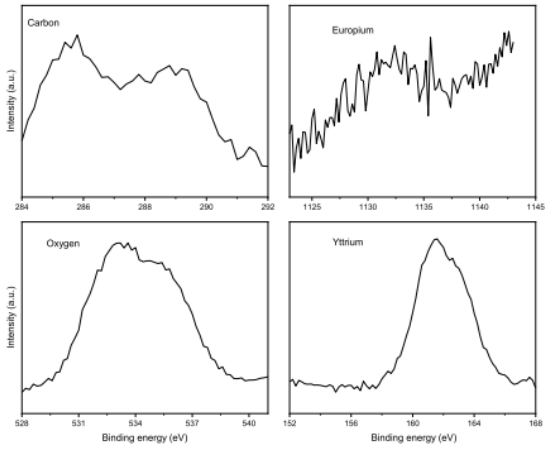

Figure 15. Individual XPS spectra for C, Eu, O and Y for $(Eu_{0.04}Y_{0.96})_2O_3$ powders after heat treatment

When compared to the as-synthesized sample, the adventitious carbon main peak in the C 1s spectrum has less intensity and asymmetry at 284.8 eV, indicating the removal of oxygenated species and combustion residues [28]. The O 1s spectrum displays a sharp, symmetric peak at 532–534 eV attributed to lattice oxygen in Y_2O_3, with minimal broadening confirming a uniform oxygen environment free of excess hydroxyls or adsorbates [25]. The Y 3d spectrum shows a sharp, intense doublet for $Y\ 3d_{5/2}$ and $Y\ 3d_{3/2}$ at 159–163 eV, confirming Y^{3+} in an ordered lattice [16]. The Eu 3d spectrum displays a well-defined signal at 1125–1140 eV for Eu^{3+}, with improved signal-to-noise ratio due to homogeneous dopant distribution and enhanced crystallinity, despite low concentration [26,30].

4. Conclusions

In this work, Y_2O_3:Eu powders were successfully synthesized via combustion synthesis and their structural, morphological, compositional, and optical properties were systematically evaluated before and after annealing at 1273 K for 30 min. Heat treatment played a crucial role in enhancing performance.

XRD confirmed low crystallinity and high lattice strain in as-synthesized powders, improving to a well-defined single-phase cubic structure matching the ICDD reference. SEM revealed a shift from highly porous, foam-like, agglomerated morphology to compact, homogeneous microstructure via densification and grain growth.

EDS, AES, and XPS verified high chemical purity (yttrium, europium, oxygen only), with reduced carbon contamination, sharper elemental signals, and enhanced Eu detection post-annealing, indicating more homogeneous dopant distribution.

Photoluminescence confirmed successful Eu^{3+} incorporation into the Y_2O_3 lattice, yielding characteristic red emission dominated by the $^5D_0 \rightarrow {}^7F_2$ transition. A 12.5-fold emission intensity increase arose from improved crystallinity, reduced defects and non-radiative centers, and optimized local Eu^{3+} environment.

These structural, chemical, and optical improvements demonstrate that annealing significantly boosts luminescent efficiency in combustion-synthesized Y_2O_3:Eu powders, highlighting post-synthesis processing for rare-earth-doped oxides in photonic and optoelectronic applications.

5. Acknowledgments

María J. Martínez-Carreón thanks SECIHTI for a postdoctoral fellowship (CVU 290939).

6. References

1. Engelsen, D. den, Ireland, T. G., Harris, P. G., Fern, G. R., Reip, P., & Silver, J. (2016). Photoluminescence, cathodoluminescence and micro-Raman investigations of monoclinic nanometre-sized Y_2O_3 and Y_2O_3:Eu^{3+}. *Journal of Materials Chemistry C*, *4*(38), 8930. https://doi.org/10.1039/c6tc02567f.
2. Saad, A. M., Ali, H., Masschelein, P., Kabbara, H., Saad, A. M., Azzouz, I. M., & Giba, A. E. (2023). Infrared to Visible Upconversion Photoluminescence from Nd-doped Yttria Ceramic for Optical Applications. *Brazilian Journal of Physics*, *53*(4). https://doi.org/10.1007/s13538-023-01303-y
3. Phan, T., Chung, D. N., Thang, P. D., Huyen, P. T., Manh, T. V., Ho, T. A., Thành, T. Đ., Vuong, N. M., Lee, B. W., & Yu, S. C. (2015). Crystal Structure and Photoluminescence Properties of Eu-Doped

Y_2O_3 Nanoparticles Prepared by Mechanical Milling. *Materials Transactions*, 56(9), 1412. https://doi.org/10.2320/matertrans.ma201556

4. Atabaev, T. Sh., Hwang, Y., & Kim, H.-K. (2012). Color-tunable properties of Eu^{3+} and Dy^{3+} codoped Y_2O_3 phosphor particles. *Nanoscale Research Letters*, *7*(1). https://doi.org/10.1186/1556-276x-7-556
5. Krauser, M. de O., Oliveira, H. H. de S., Cebim, M. A., & Davolos, M. R. (2018). Relationship between scintillation properties and crystallite sizes in Y_2O_3:Eu^{3+}. *Journal of Luminescence*, *203*, *100*. https://doi.org/10.1016/j.jlumin.2018.06.038
6. Scarafagio, M., Tallaire, A., Tielrooij, K., Cano, D., Grishin, A. E., Chavanne, M., Koppens, F. H. L., Ringuedé, A., Cassir, M., Serrano, D., Goldner, P., & Ferrier, A. (2019). Ultrathin Eu- and Er-Doped Y2O3 Films with Optimized Optical Properties for Quantum Technologies. *The Journal of Physical Chemistry C*, *123*(21), 354. https://doi.org/10.1021/acs.jpcc.9b02597
7. Falcony, C., Aguilar-Frutis, M., & García-Hipólito, M. (2018). Spray Pyrolysis Technique; High-K Dielectric Films and Luminescent Materials: A Review. *Micromachines*, *9*(8), 414. https://doi.org/10.3390/mi9080414
8. Renu, Mor, N., Jitender, Dahiya, B., & Dahiya, H. (2026). Photo-physical attribute of red-emissive Y_2O_3:Eu^{3+}: Bi^{3+} application in anti-counterfeiting, latent fingerprints, and transparent-flexible noncrystalline encased in PVA/CS film. *Journal of Materials Science Materials in Electronics*, *37*(7). https://doi.org/10.1007/s10854-026-16881-1
9. Yadav, R. V., Verma, R., Kaur, G., & Rai, S. B. (2012). Change in structural morphology on addition of ZnO and its effect on fluorescence of Yb^{3+}/Er^{3+} doped Y_2O_3. Spectrochimica Acta Part A Molecular and Biomolecular Spectroscopy, 103, 216. https://doi.org/10.1016/j.saa.2012.10.054
10. Du, P., Guo, Y., Lee, S. H., & Yu, J. S. (2017). Broad near-ultraviolet and blue excitation band induced dazzling red emissions in Eu^{3+}-activated Gd_2MoO_6 phosphors for white light-emitting diodes. *RSC Advances*, *7*(6), 3170. https://doi.org/10.1039/c6ra25652j
11. Xin, M. (2018). Effect of Eu doping on the structure, morphology and luminescence properties of ZnO submicron rod for white LED applications. *Journal of Theoretical and Applied Physics*, *12*(3), 177. https://doi.org/10.1007/s40094-018-0304-1
12. Ritter, B., Krahl, T., Rurack, K., & Kemnitz, E. (2014). Nanoscale CaF2 doped with Eu3+ and Tb3+ through fluorolytic sol–gel synthesis. *Journal of Materials Chemistry C*, *2*(40), 8607. https://doi.org/10.1039/c4tc01073f
13. Slimen, F. B., Zaâboub, Z., Haouari, M., Mohamed, N. B. H., Ouada, H. B., Chaussedent, S., & Gaumer, N. (2017). Effect of CdS nanocrystals on the photoluminescence of Eu3+-doped silicophosphate sol gel glass. *RSC Advances*, *7*(24), 14552. https://doi.org/10.1039/c7ra01313b
14. Vukovic, O., Folpini, G., Wong, E. L., Leoncino, L., Terraneo, G., Albaqami, M. D., Petrozza, A., & Cortecchia, D. (2023). Structural effects on the luminescence properties of CsPbI3 nanocrystals. Nanoscale, 15(12), 5712. https://doi.org/10.1039/d2nr06345j
15. Wincukiewicz, A., Mech, W., Grankowska, S., Wołoś, A., Drabińska, A., Słupiński, T., Korona, K. P., & Kamińska, M. (2018). Radiative recombination and other processes related to excess charge carriers, decisive for efficient performance of electronic devices. *Lithuanian Journal of Physics*, *58*(1). https://doi.org/10.3952/physics.v58i1.3651
16. Sotiriou, G. A., Schneider, M., & Pratsinis, S. E. (2010). Color-Tunable Nanophosphors by Codoping Flame-Made Y2O3 with Tb and Eu. *The Journal of Physical Chemistry C*, *115*(4), 1084. https://doi.org/10.1021/jp106137u
17. Dhaterwal, D., Matoria, M., Dalal, A., Kumar, S., & Singh, S. (2024). Synthesis and Characterization of Color Tunable Europium(III) and Terbium(III) Co-Doped $LaSrAl_3O_7$ Nanocrystalline Phosphors: A PL Synergy. *Asian Journal of Chemistry*, *36*(8), 1933. https://doi.org/10.14233/ajchem.2024.32115
18. Matsumoto, S., Watanabe, T., & Ito, A. (2022). Photo- and Radioluminescence Properties of Eu3+-doped Y2O3 Thick Film Phosphor Prepared via Chemical Vapor Deposition. *Sensors and Materials*, *34*(2), 669. https://doi.org/10.18494/sam3698
19. Eibl, M., Shaw, S., Prieur, D., Roßberg, A., Wilding, M. C., Hennig, C., Morris, K., Rothe, J., Stumpf, T., & Huittinen, N. (2020). Understanding the local structure of Eu^{3+}- and Y^{3+}-stabilized zirconia: insights from luminescence and X-ray absorption spectroscopic investigations. *Journal of Materials Science*, *55*(23), 10095. https://doi.org/10.1007/s10853-020-04768-3
20. Lal, S. C., Naseemabeevi, J. I., & Ganesanpotti, S. (2020). Distortion induced structural characteristics of $Ba_2R_{2/3}TeO_6$(R = Y, Gd, Tb, Dy, Ho, Er, Tm, Yb and Lu) double perovskites and their multifunctional optical properties for lighting and ratiometric temperature sensing. *Materials Advances*, *2*(4), 1328. https://doi.org/10.1039/d0ma00471e
21. Ruiz-Fuertes, J., Gomis, O., León-Luis, S. F., Schrodt, N., Manjón, F. J., Ray, S., Santamaría-Pérez, D., Sans, J. A., Ortiz, H. M., Errandonea, D., Ferrer-Roca, Ch., Segura, A., Martínez-García, D., Lavín, V., Rodríguez-Mendoza, U. R., & Muñoz, A. (2015). Pressure-induced amorphization of YVO_4:Eu^{3+}nanoboxes. *Nanotechnology*, *27*(2), 25701. https://doi.org/10.1088/0957-4484/27/2/025701

22. Colomer, M. T., Díaz-Moreno, S., Tamayo, A., Ortiz, Á. L., & Chaboy, J. (2018). An interplay between electronic and structural effects on the photoluminescence decay mechanisms in $LaPO_4 \cdot nH_2O:Tb^{3+}$ and $LaPO_4:Tb^{3+}$ single-crystal nanorods. *Journal of Materials Chemistry C*, *6*(46), 12643. https://doi.org/10.1039/c8tc03187h
23. Reddy, L. (2024). The Role of Anions in Rare-earth Activated Inorganic Host Materials for its Luminescence Characteristics. *Journal of Fluorescence*. Springer Science+Business Media. https://doi.org/10.1007/s10895-023-03561-0
24. Jacobsohn, L. G., Tappan, B. C., & Muenchausen, R. E. (2008). The effect of hydrostatic pressure on the combustion synthesis of Y_2O_3:Bi nanophosphor. *OSTI OAI (U.S. Office of Scientific and Technical Information)*. https://www.osti.gov/biblio/960904
25. Siddique, F., González-Cortés, S., Mirzaei, A., Xiao, T., Rafiq, M. A., & Zhang, X. (2022). Solution combustion synthesis: the relevant metrics for producing advanced and nanostructured photocatalysts. *Nanoscale*, *14*(33), 11806. Royal Society of Chemistry. https://doi.org/10.1039/d2nr02714c
26. Kitagawa, Y., Ueda, J., & Tanabe, S. (2024). A brief review of characteristic luminescence properties of Eu3+ in mixed-anion compounds. *Dalton Transactions*, *53*(19), 8069. https://doi.org/10.1039/d4dt00191e
27. Marlière, C. (1994). Contribution to the study of ultra-thin metallic layers: Structural, electrical and magnetic properties. *HAL (Le Centre Pour La Communication Scientifique Directe)*. https://tel.archives-ouvertes.fr/tel-00007871
28. Miyoshi, K., and Buckley, D. H. (1982). Adhesion and friction of transition metals in contact with non-metallic hard materials. *Wear*, *77*(2), 253. https://doi.org/10.1016/0043-1648(82)90109-0
29. Denis, Y., Elissalde, C., Suchomel, M. R., Gayot, M., Weill, F., Labrugère, C., Etienne, L., Vaudescal, M., Cam, N., Chung, U.-C., Reverón, H., Chevalier, J., Beauvoir, T. H. de, Estournès, C., Aymonier, C., & Philippot, G. (2023). Continuous Flow Synthesis of Yttria-Stabilized-Zirconia Nanocrystals in Supercritical Solvothermal Conditions. *Advanced Materials Technologies*, *9*(3). https://doi.org/10.1002/admt.202301474
30. Benti, H. G., Woldeyohannes, A. D., & Yigezu, B. S. (2022). Improving the Efficiency of Cutting Tools through Application of Filtered Cathodic Vacuum Arc Deposition Coating Techniques: A Review *Advances in Materials Science and Engineering*, *2022*, 1. Hindawi Publishing Corporation. https://doi.org/10.1155/2022/1450805
31. Chang, C. C. (1971). Auger electron spectroscopy. *Surface Science*, *25*(1), 53. https://doi.org/10.1016/0039-6028(71)90210-x